Improving the Circularization Efficiency, Stability and Translatability of Circular RNA by circDesign

Congcong Xu[1,†], Liang Zhang[2,†], Weiyun Wang[1,†], Yuying Tang[1], Qiuhe Wang[1], Jinqi An[1], Heng Xu[1], Yun Ge[1], Hanfei Zhu[1], He Wang[1], Bin Li[1], Xiaotiao Wang[1], Xuhui Qiu[1], Mingyun Shen[1], Geng Chen[1], Haifa Shen[1, $], Liang Huang[3, $], Hangwen Li[1,4, $]

[1]StemiRNA Therapeutics, Shanghai, China
[2]China Pharmaceutical University, Nanjing, China
[3]Coderna.ai, Sunnyvale, CA, USA
[4]Shanghai East Hospital, Shanghai, China

[$]Correspondence to:

Liang Huang (liang.huang.sh@gmail.com)
Haifa Shen (shf@stemirna.com)
Lead contact: Hangwen Li (lihangwen@stemirna.com)

†These authors contributed equally.

Abstract

Synthetic circular RNA (circRNA) has recently emerged as the next generation RNA technology for vaccine and drug development, featuring its uniqueness in a closed-loop structure and cap-independent translation mechanism. However, rational design and optimization of circRNA to improve its stability and protein coding potential remains challenging due to lack of structure prediction tool and sequence design algorithm for endless circular-shaped RNA. In this study, we presented circDesign, a computational approach to achieve optimal design of the circRNA with enhanced circularization efficiency, stability, and translatability. Using rabies virus glycoprotein (RABV-G) and varicella-zoster virus (VZV) glycoprotein gE as the exemplified antigens, we demonstrated that optimized circRNAs encoding corresponding antigens exhibited higher stability and protein translation efficiency *in vitro*. Formulated by proprietary delivery system lipopolyplex (LPP), the optimized circRNA vaccines encoding RABV-G or VZV gE antigen further elicited enhanced humoral and cellular *in vivo* immune responses in mice. Taken together, this circular RNA design approach provided a general strategy to leverage the capability of circRNA as next generation vaccines or therapeutics.

Keywords: circular RNA; circDesign; Algorithm; RNA vaccine; Rabies vaccine; Varicella-zoster virus vaccine; Lipopolyplex

Introduction

Rational sequence design of messenger RNAs (mRNAs) is of pivotal importance to maximize the potency of mRNA vaccines or therapeutics[1]. Optimization of conventional linear mRNA usually involves 5'- & 3'-untranslated region (UTR) and open reading frame (ORF), which could be simply achieved by combining naturally occurring UTR pair with codon optimized ORF region[2, 3]. As exemplified by Moderna's mRNA-1273 and BioNTech's BNT162b2 COVID-19 mRNA vaccines, the optimized ORF was directly flanked with previously screened UTR pair[4]. Besides, it was reported the functional half-life of mRNA dictates its *in vivo* performance as the translation efficiency and stability of mRNA synergistically impact the protein output[5, 6]. To achieve enduring and efficient translation, the ORF sequence should be optimized towards more stable secondary structure without compromising its codon preference.

Recent advancement in circRNA demonstrated its potentials as next generation vaccines or therapeutics owing to its uniqueness in endless structure distinct from linear mRNA[7-9]. Other than ORF region, synthetic circRNA usually contains internal ribosome entry site (IRES) motif upstream of ORF for translation initiation[10]. The correct folding of IRES as a functional motif to recruit translation pre-initiation complex (PIC) is a prerequisite of efficient translation of circRNA[11]. However, due to the lack of structure prediction tool for circular RNA, along with insufficient understanding of the crosstalk between IRES and ORF regions on circRNA, current sequence optimization of circRNA heavily relied on modular screening[12]. This independent ORF optimization on circRNA without considering the backbone sequence including IRES motif and residual regions as a whole introduces more uncertainties in the process of circRNA sequence optimization.

Here we present an efficient approach called circDesign based on previously reported LinearDesign algorithm[6] to generate optimized circRNA sequences for rabies and VZV vaccine development. In brief, a pool of candidate ORFs were firstly generated using LinearDesign algorithm based on optimization of codon usage and minimum free energy (MFE). By assembly of ORF with IRES motif as well as other functional regions, the positional entropy and ensemble diversity were evaluated aside from overall MFE and codon adaptation index (CAI)[13-15]. To evaluate the impact of these parameters on circRNA performance, we performed *in vitro* and *in vivo* characterization of these circRNAs compared to conventionally optimized ORF sequences, it demonstrated greater performance in terms of circularization, stability, protein translation as well as *in vivo* immune responses. The circDesign approach provides a general strategy for protein-coding circular RNA design and potentially enables broader circRNA-based vaccine and therapeutic development.

Results

circDesign approach for circular RNA design

To implement circDesign for circRNA-based rabies vaccine design, the ORF region encoding RABV-G[16, 17] was designed such as to achieve efficient and prolonged expression. Different from linear mRNA design which is composed of relatively short functional elements (~ 100 nt in length) including 5'-UTR and 3'-UTR, artificially constructed circular RNA with protein translation capacity usually contains long viral or cellular IRES sequence (500-800 nt in length) for cap-independent translation[10, 18, 19]. More importantly, the IRES region needs to be independently folded into a hierarchical structure without interference from other sequence as to efficiently recruit translational PIC. Therefore, a key consideration in circDesign involves mitigating the cross-interaction of ORF region with IRES motif, thus facilitating the formation of functional IRES with high confidence. Moreover, following a permuted intron-exon (PIE) circularization[20], residual exon fragments on circularized RNA is redundant and introduced more uncertainties to the function of circRNA as this element may interfere with the folding of other elements. As such, precautions must be taken when optimizing the ORF of circRNA since functional IRES motif and residual exons are present in the sequence.

In this study, the circDesign approach consisted of four integral steps as illustrated in **Fig. 1a**. In brief, the first step involves the implementation of LinearDesign algorithm to generate a pool of ORF candidates. Followed by the screening of ORF based on CAI and MFE, the stability and translation efficiency were carefully considered. Then a completed circular RNA was assembled with other necessary residual fragments including IRES, exons and spacers. In addition, the positional entropy of IRES and ensemble diversity of circRNA were evaluated. Lower positional entropy suggests a more conserved structure of IRES, while a lower ensemble diversity indicates a higher consistency and predictability of the circRNA structure, both of which contribute to higher structure stringency[21, 22]. In addition, the inter-region and intra-region interaction was evaluated primarily aiming to mitigate the impact from ORF on the independent folding of IRES, which is critical for efficient translation initiation. Based on the abovementioned screening process, the designed circRNAs were then subjected to *in vitro* and *in vivo* evaluation for screening.

Design, synthesis, and characterization of circular RNA encoding RABV-G

Herewith RABV-G encoding circRNA, we designed six ORFs, along with two benchmark sequences. The six circDesign-generated designs are widely dispersed in the low-MFE regions (**Fig. 1b**). To better understand the impact of MFE and

CAI in terms of biological implications, following the LinearDesign's experimental design principle, we crafted sequences with nearly identical values in MFE (CR2, CR3 // CR4, CR5) or in CAI (CR5, CR6, CR-Ther // CR1, CR2, CR-Novo). Benchmark ORF sequences (CR-Ther and CR-Novo) were designed with publicly available platforms from Thermo Fisher and Novoprotein respectively, which primarily optimized the codon preference without considering the secondary structure. The color darkness of each sequence represents the ensemble diversity of assembled circular RNA. As suggested, the ensemble diversity of designed circRNA is correlated with MFE. With a lower MFE of ORF region, the ensemble diversity of circRNA was lowered, suggesting a more well-defined structure with independent folding of each region.

To synthesize the circRNA, the circularization of RNA was mediated by self-cleaving permuted group I catalytic intron which was separated into 5'-intron and 3'-intron in the original sequence design as previously reported[7, 20]. In brief, both ends of linear mRNA consisted of complementary homology arms facilitating the folding of active ribozyme structure, thus undergoing two constitutive transesterification reactions to form junction between two exon fragments (E1 & E2). In this study, IRES from Coxsackievirus B3 (CVB3)[23, 24] was adopted upstream of open reading frame (ORF) to drive the protein translation process. As shown in the **Fig. 1b**, different ORF embedded in the linear mRNA design could be incorporated in circular RNA *via* the same circularization reaction. Taking CR3 and CR-Novo as representative sequences, the ORF of CR3 was designed with much lower MFE and less inter-region interaction with IRES motif compared to CR-Novo. As shown in **Fig. 1c**, though with the same backbone sequence and amino acid sequence, most of the amino acid could be coded by different synonymous codons, resulting in numerous sequence design space. The secondary structure of CR3 and CR-Novo was predicted as **Fig. 1d**. It was clear that the same IRES region (light grey color) had distinct folding in two circRNAs. The secondary structure folding prediction of circRNA rabies sequences (see **Extended Data. 1&2**) demonstrated that suboptimal ORFs (Ther and Novo) may disrupt the correct folding of IRES. And the pairwise visualization of these two circRNA (**Fig. 1e**) showed that CR-Novo had more inter-region base pairing (red connecting line) than that of CR3. The base pairing in CR3 mainly led to intra-region folding (blue connecting line). Same results were obtained in other circDesign-based sequences (see **Extended Data. 3&4**).

As a result of the difference in MFE, CAI value and ensemble diversity, the circularization efficiency varied among these sequences. Considering a more compact ORF region folding with less interference with the formation of active intron, circDesign-generated sequences (CR1-6) had relatively higher circularization efficiencies than those of CR-Novo and CR-Ther (**Fig. 2a**). To remove impurities from the circularization reaction products, size-exclusion

column chromatography was used to obtain purified circRNA (see **Extended Data. 5a**) which induced minimized innate immunogenicity (see **Extended Data. 5b-c**). To characterize the circRNA, non-denaturing agarose gel electrophoresis was performed at room temperature. As shown in **Fig. 2b**, it's intriguing to find that the gel mobility of circRNAs was well correlated with their MFE values given their same nucleotide length. CR-Novo sequence, with the highest MFE, exhibited the slowest mobility in the gel matrix possibly due to its less compact structure, while circDesign-generated sequences especially CR1-5 had faster migration as a result of their highly compact folding structure. This suggested the potential of optimizing ORF sequences of circRNA in regulating their folding paradigm.

Optimized circRNA exhibited enhanced *in vitro* stability

As the secondary structure dictates the functionally half-life of mRNA[5], we then extensively evaluated the *in vitro* stability of circRNAs in terms of thermodynamic folding, in-solution degradation as well as intracellular decay. By heating the circRNA in solution to gradually unfold its structure, the fluorescence intensity from RNA bound RiboGreen® reagent attenuated accordingly. We calculated the melting temperature (T_m) of circRNA from the fluorescent intensity curve as **Fig. 2c**. CR1-3 had slightly higher T_m than CR4-6, with an obviously increased thermodynamic stability compared to CR-Novo and CR-Ther. The melting curve results was associated with MFE values.

Like linear mRNA, the chemical instability of circRNA originated mainly from hydrolysis reaction despite of its endless structure[25-27]. To examine the in-solution stability of all circRNAs, RNA samples were incubated in PBS buffer containing 10 mM Mg^{2+} at 37 °C mimicking the physiological buffering system over a time course of 60 h. At different time points, the integrity of circRNA was assessed. The degradation of circRNA as a function of time was fitted to a one-phase decay curve, suggesting different degradation kinetics. circRNAs with higher MFE values (CR-Novo & CR-Ther) underwent faster degradation kinetics with half-life ($t_{1/2}$) of 9.14h and 9.68h respectively, while CR1-3 had considerably extended $t_{1/2}$ ranging from 15.56 to 20.62 h (**Fig. 2d**).

Apart from chemical degradation, the intracellular decay of exogenous circRNA is also regulated by different pathways in related to its translational activity[28, 29]. To assess the in-cell half-life of circRNA, the abundance of circRNA extracted from cells was quantified using reverse transcription quantitative real-time PCR (RT-qPCR) method at various time points (3, 12, 24, 48 and 72h) post-transfection into Human Skeletal Muscle Cells (HSkMC). As illustrated in **Fig 2e**, a slightly different decay pattern of all tested circRNA was observed. CR1 and CR3 had a prolonged intracellular half-life (24.34 h and 19.31 h, respectively) while CR-

Novo and CR5 showed a faster in-cell decay (10.21 h and 9.18 h, respectively). As the biological fate of transfected circRNA is associated with a plethora of factors including translation status and nuclease resistance[30, 31], the in-cell degradation of artificially synthesized circRNA could possibly be controlled by tuning its secondary structure and translation efficiency. We reasoned that CR3 sequence had decent stability in conjunction with high translation efficiency, enabling its resistance against chemical degradation and biological decay.

circDesign improved the protein coding capacity of circRNA

Since the stability and translation efficiency of circRNA co-regulates the protein output level, we evaluated the RABV-G expression from transfected circRNA in HSkMC using flow cytometry (**Fig. 2f**). To gain thorough comparison, we included conventional chemically modified linear mRNA harboring Novo ORF encoding RABV-G as a control group as well. At 24 h post-transfection, antigen was highly expressed in CR3 group as suggested by the mean fluorescent intensity (MFI). CR1-5 had a remarkably higher protein output level than CR6 and CR-Ther, largely attributed to the relatively instable structure of CR6 and CR-Ther. However, it's interesting to find that benchmark CR-Novo exhibited a decent protein coding capacity despite of its lower CAI value compared to CR-Ther. This evidence emphasized the importance of taking multiple influential factors into consideration other than CAI to stratify the mRNA coding potentials. Moreover, we found that the circular form (CR-Novo) outcompeted its linear counterpart (LR-Novo) in protein translation level (**Fig. 2f**), where stability factor might be the major contributing factor as these two forms of RNA shared the same CAI of ORF. The correlation analysis of in-solution and in-cell half-life with MFE (**Fig. 2g**) showed the importance of MFE parameter in improving circRNA half-life. Predicted half-life correlated well with the observed experimental data (**Fig. 2h**).

To elucidate the underlying mechanism of enhanced protein expression in relation to structure (**Fig. 3a&b**), we performed ribosome profiling[32] and polysome profiling[33] analysis of CR3 and CR-Novo for side-by-side comparison. Following the standard workflow (**Fig. 3c**) after transfection into cells, the ribosome footprints were aligned to the full-length CR3 and CR-Novo, respectively. The ultracentrifugation fractions were quantified to determine the fractional composition of circRNA. In both RNA direct sequencing counts and ribosome sequencing counts (**Fig. 3d**), the CR3 had higher fpkm (fragment per kilobase of transcript per million mapped reads) of RNA-seq and ribo-seq than that of CR-Novo at the time of cell being harvested, indicating a higher circRNA abundance and ribosome footprints of CR3. Footprint abundance relative to mRNA abundance dictates the TE (translation efficiency) [34] of circular RNA. The TE of CR3 (233.7) was calculated as 1.5-fold of CR-Novo (159.9), suggesting a markedly higher translation efficiency from circDesign optimized CR3. After alignment of the ribosome footprints on circRNA, it's clear that the cap-

independent translation mechanism of circRNA driven by CVB3 IRES efficiently recruits ribosome onto circular RNA to initiate the protein translation. Most of the ribosome protected fragments were identified in ORF region in both CR3 and CR-Novo, though the read count and distribution varied between these two groups. As suggested in **Fig. 3e**, the ribosomal footprints were mapped and distributed more evenly throughout the ORF region while CR-Novo had more distinct footprint accumulation peaks. The fully aligned ribosomal footprints were plotted on circular CR3 and CR-Novo annotated with each functional regions, respectively (**Extended Data. 6**). In addition, several major peaks upstream of ORF indicated the recruitment of ribosome for translation initiation. Taking a closer look at the secondary structure and pairwise visualization (**Extended Data. 7**), it's highly possible that the disrupted IRES motif in CR-Novo impeded the translational machinery recruitment, thus resulting in a much lower ribosome footprint abundance.

In addition, polysome profiling was performed on CR3 and CR-Novo to compare the ribosome loading capacity. Ultracentrifugation of both CR3 and CR-Novo was successful as shown in **Fig. 3f**, which quantified the total RNA in each fractional position. 80S fraction referred to monosome and later peaks referred to polysome-bound circRNA. By further quantifying the CR3 or CR-Novo in each collected fractions, we observed a higher ribosome loading in CR3 compared to CR-Novo (**Fig. 3g**).

LPP delivery system efficiently delivered circRNA *in vitro* and *in vivo*

To investigate the performance of circRNA *in vivo*, a proprietary lipopolyplex (LPP) delivery system[35, 36] was used to formulate the circular RNA. As shown in **Fig. 4a**, following a two-step microfluidic mixing process, cationic polymer complexed circRNA could be encapsulated in a bilayer liposome-like nanoparticle with a "core-shell" structure. Previous studies have demonstrated the efficiency and safety of using this LPP delivery system to deliver linear mRNA[37, 38]. Herewith circRNA encoding GFP (CR-GFP) or firefly luciferase (CR-FLuc) was formulated into LPP to study its *in vitro* cell expression and *in vivo* biodistribution compared to its chemically modified linear counterpart (LR-GFP or LR-FLuc), respectively. Flow cytometry analysis of cells treated with LPP formulated CR-GFP showed a dosage-dependent translation from 50 ng, 200 ng to 500 ng per well in a 6-well plate. Stronger expression was observed in circular RNA group than that of LR-GFP (**Fig. 4b**). Besides, the protection of encapsulated circRNA against RNase digestion was evaluated in LPP and lipid nanoparticle (LNP), a widely used mRNA delivery system. The residual circRNA was quantified at 30 min post-treatment and the results suggested a higher protection efficacy against nuclease digestion using LPP formulation.

Upon intramuscular administration of LPP formulated CR-FLuc and LR-FLuc in

mice, *in vivo* imaging system (IVIS) captured the whole-body *in vivo* luminescence activities at different time points (6, 24, 48, 72, 96 and 168 h) (**Fig. 4d**), reflecting the expression kinetics of luciferase from CR-FLuc or LR-FLuc. It turned out that circular RNA produced luciferase in a more durable manner with higher accumulated expression as shown in **Fig. 4e**. Though with similar physicochemical properties of LPP formulation (**Extended Data. 8a**) and lower onset expression as seen at 6 h post administration, CR-FLuc showed extended expression over the course of one week while luminescence from LR-FLuc group descended to background level within a relatively shorter time (2 days post-dosing). A gross estimation of accumulated expression was conducted simply by calculating the area-under-curve (AUC) of total flux of luminescence. CR-FLuc group led to approximately 5.3-fold of total luciferase expression compared to its linear counterpart over the course of 8 days (**Fig. 4f**). Indeed, other group has reported similar translation kinetics of circular RNA compared to linear mRNA[12], thus rendering circRNA a promising therapeutic or vaccine platform for sustained protein supplement or enduring protection against pathogens. These results suggested the feasibility of using LPP for efficient *in vivo* delivery of circRNA despite of its closed loop feature.

circDesign optimized circRNA rabies vaccine demonstrated superior *in vitro* stability and *in vivo* performance

It has been reported that linear mRNA encapsulated in lipid nanoparticles still underwent slow transesterification hydrolysis[25]. In this study, the stability of LPP-circRNA nanoparticles was evaluated to simulate the vaccine storage condition under the formulated situation. Henceforth, the same lipid composition was adopted to encapsulate circDesign-optimized CR1-6 and benchmark circRNA encoding RABV-G to rule out the impact from delivery system on their *in vitro* and *in vivo* performance. The *in vitro* characterization of formulated circRNAs showed that LPP nanoparticles had similar size of around 110 nm (**Fig. 4g**) and positive zeta potentials (in the range of 20-35 mV) (**Fig. 4h**) regardless of the encapsulated circRNA. However, the importance of optimizing the stability of circRNAs was manifested in their storage stability in lipid formulation. We examined the mRNA content of LPP-circRNA complex on day 30 at room temperature to assess the integrity of RNA component. A faster RNA degradation in LPP formulated CR-Novo and CR-Ther was observed (**Fig. 4i**) with 15-20% circRNA loss on day 30 while circDesign optimized circRNAs (CR1-5) showed little degradation over tested period. Moreover, the in vitro innate immunogenicity and cell cytotoxicity was evaluated with LPP formulated circRNAs compared to linear RNA (**Extended Data. 8b&c**). Minimal *in vitro* innate immunogenicity and cell toxicity was observed for SEC purified circRNAs formulated by LPP.

We then evaluated the *in vivo* immunogenicity of RABV-G encoded RNA

374 vaccines. By intramuscular injection into mice, it's proposed that the circRNA-
375 LPP nanoparticles entered antigen-presenting cells *via* endocytic pathway and
376 circRNA got released from endosome into cytoplasm for antigen translation. The
377 translated antigens were then processed to elicit humoral and cellular immune
378 responses as illustrated in **Fig. 5a**. Two doses of rabies vaccines were *i.m.*
379 administered at an interval of two weeks in balb/c mice (n=5 per group). Mice
380 were weighted after first dosing and no weight loss was observed for both
381 circRNA and linear RNA group (**Extended Data. 8d**). Mice sera were collected
382 on day 10, 14, 21 & 28 to assess the pseudovirus neutralizing antibody titer
383 (pVNT) and spleens were extracted for cellular immunity assessment on day 28
384 (**Fig. 5a**). As neutralizing antibodies (nAbs) play a critical role in protection
385 against rabies virus[39], monitoring the geometric titer (GMT) nAb level gave us a
386 hint on the efficacy of rabies vaccines. In this study, linear mRNA encoding the
387 same ORF (LR-Novo) as CR-Novo was used for comparison as well. On day 10
388 post-priming dose, LR-Novo elicited a slightly higher antibody titer compared to
389 all circRNA groups possibly due to relatively faster onset expression of antigens,
390 though overall titers remained low (**Fig. 5b**). Slower but durable antigen
391 expression induced comparable immune responses among circRNA groups while
392 CR1, with the lowest MFE, had 2-fold pVNT of LR-Novo and 4-fold pVNT of
393 CR-Novo (**Fig.5c**). One week after booster (day 21), circDesign-optimized
394 sequence groups (CR1-4) elicited much stronger humoral immune responses than
395 the rest of groups (CR5-6, CR-Novo, CR-Ther and LR-Novo) (**Fig. 5d**). Of note,
396 all circular RNA groups exhibited continued increase in pVNTs on day 28,
397 whereas linear RNA had no further enhancement in antibody titer (**Fig. 5e**). The
398 geometric increase (GMI) of pVNT was calculated based on the GMT on day 10
399 as baseline to show the trend of humoral immune response induction. As plotted
400 in **Fig. 5f**, LR-Novo had the least GMI trend while CR1&3 showed durable
401 induction of immune responses. The pVNT kinetics of each group as a function
402 of time were summarized as **Fig. 5h**, suggesting the great potentials of circDesign-
403 enabled vaccine design in triggering strong antibody responses. It's worth noting
404 that cellular immune responses induced by circDesign optimized sequences
405 (CR1-4) especially CR3 are more prominent than other groups (**Fig. 5g**). A higher
406 frequency of RABV-G specific T cells secreting interferon γ (IFN-γ) was observed
407 in CR3 group with a mean value of 280.1 spots counted using Enzyme-linked
408 immunosorbent spot (ELISpot) assay (**Extended Data. 9**). Though the practical
409 significance of higher RABV-G specific cellular immunity in rabies prevention
410 remains elusive[40, 41], we speculate the improved T cell immune responses from
411 circDesign optimized vaccine may play important roles in rabies virus clearance
412 from the host[40]. Taking a closer look at the cellular immune activation profile,
413 flow cytometry analysis of the RABV-G peptide stimulated T cells was performed.
414 Following a stepwise gating of the cell population (**Extended Data. 10**), the ratio
415 of $CD4^+$ and $CD8^+$ T cells producing IFN-γ, TNF-α, IL-2 and IL-4 were computed,
416 respectively. The results indicated the strong RABV-G specific $CD4^+$ and $CD8^+$ T

417 cell responses elicited by circDesign generated vaccines (**Extended Data. 11**).
418 We observed higher ratios of IFN-γ, TNF-α and IL-2 secreting T cells but minimal
419 IL-4 producing population in both $CD4^+$ and $CD8^+$ T cells (**Extended Data. 11**),
420 suggesting a T_h1-biased immune responses induced by circRNA rabies vaccines.
421
422 Combined with the in-solution and in-cell stability results of naked or LPP
423 formulated circRNA, these results convincingly demonstrated the improved
424 potency from circDesign-optimized sequences owing to their well-defined
425 structure and enhanced stability during storage and intracellular trafficking. The
426 correlation analysis of *in vivo* pVNT and ELISpot on day 28 showed the relation
427 to MFE of circRNA (**Extended Data. 12**).
428
429 **The durable humoral immune response may be related to the *in vivo* stability**
430 **of CR3**
431
432 The abovementioned *in vitro* and *in vivo* evaluation of circRNAs implicated the
433 importance of circRNA stability as well as translation efficiency in achieving
434 optimal performance. Therefore, balancing the optimization of CAI (translation
435 efficiency) and MFE (stability) with a well-defined circRNA folding structure
436 might synergistically contribute to a top performer sequence, thus leading to
437 maximized *in vivo* outcomes. Of all circDesign optimized sequences, CR3
438 showed superior stability, protein translation output, along with *in vivo*
439 immunogenicity (See **Extended Data Table 1** for summarized assessment
440 results). Compared to CR-Novo, it's intriguing to find that another benchmark
441 sequence CR-Ther had lower protein translation and induced relatively weaker
442 immune responses despite its higher CAI. Consequently, we further compared
443 CR-Novo with CR3 regarding their *in vivo* stability to explain the advantages of
444 circDesign-generated CR3 over CR-Novo in their potency and durability. To
445 study the *in vivo* stability, LPP formulated CR3 and CR-Novo were *i.m.*
446 administered into balb/c mice (n=5 per group). At 6, 24, 48, 72 and 168 h post-
447 dosing, mice were sacrificed and total RNAs were extracted from different organs
448 including muscle (injection site), lymph node, spleen, liver, lung, heart, kidney,
449 brain and small intestine (sm. int.). A standard plasmid containing the target
450 sequence was used as internal standard control to quantify the circRNA copies per
451 μg of total RNA using qPCR analysis. The biodistribution results revealed the
452 good safety profile of LPP delivery system, as major injected dose accumulated
453 at the injection site without significant retention in liver both for CR3 (**Fig. 6b**)
454 and CR-Novo (**Fig. 6a**). Moreover, as time went by, more fractions of circRNA
455 were detected in spleen and lymph node where the immune activation mainly
456 occurs. It's noted that CR3 had extended muscle retention proportion (88.5%, 70%
457 and 29.4% at 24h, 48h and 72h, respectively) compared to CR-Novo (74.5%, 25.4%
458 and 7.4% at 24h, 48h and 72h, respectively) (**Fig. 6c**). The comprehensive
459 quantification data were summarized in **Extended Data Table 2**. It's hypothesized

that higher *in vivo* stability of CR3 benefited the longer retention at injection site given the same dosage as CR-Novo. Within 72 h of administration, the circRNA quantification data of muscle at injection site suggested the higher abundance of CR3 (**Fig. 6d**). This potentially contributed to a sustained lymphatic migration of antigen presenting cells (APCs) to peripheral immune organs such as draining lymph nodes and spleen, leading to robust immune activation.

The long-lasting humoral immune response induced by circDesign optimized rabies vaccine

Above findings rendered CR3-LPP a more potent rabies vaccine candidate potentially inducing long-lasting adaptive immunity against rabies virus. To study the longevity of immune responses, balb/c mice (n=5 per group) were immunized with LPP formulated CR3 and CR-Novo with the same dosage (2 μg per immunization for prime and boost at an interval of two weeks). The mice sera were collected over a much longer period during which the nAb titer was monitored (**Fig. 6e**). As shown in **Fig. 6f**, CR3 induced a stronger humoral immune response following prime and booster. 14 days after booster dose (on day 35), the pVNT of CR3 group remained 1.7-fold of CR-Novo (**Fig. 6f**). With a relatively slower waning rate of pVNT, CR3 group exhibited 2.1-fold and 3.2-fold pVNT over CR-Novo group on day 90 and 163, respectively. According to the guidelines of rabies vaccine released by World Health Organization (WHO), a second booster was recommended when re-exposure to rabies virus occurred 3 months after the last booster[42]. Thus, we administered the second booster in mice on day 163 to evaluate the immune responses after re-boost. The second booster induced much stronger immune response in CR3 group with 4.6-fold and 3.9-fold pVNT of CR-Novo one week (day 170) and two weeks (day 177) after re-booster dose (**Fig. 6f**). Besides, the cellular immune responses were assessed by ELISpot on day 170 using mice spleenocytes. CR3 immunized mice had shown significantly stronger antigen-specific IFN-γ and TNF-α secretion, potentially leading to better clinic outcome.

Second antigen demonstrating the robustness of circDesign in optimizing circRNA for improved performance

The *in vitro* and *in vivo* results of circRNA encoding RABV-G demonstrated the usefulness of circDesign algorithm in circular RNA sequence design. Considering the potential applicability of circDesign for different circRNA design and optimization, we validated the robustness of this algorithm using varicella-zoster virus (VZV) glycoprotein E (gE) as a second antigen to develop circRNA-based vaccine. At the same time, a new self-cleaving ribozyme from *Azoarcus* pre-tRNA was adopted to mediate the circularization reaction (See Supplementary materials for sequence details).

Though with a different intron splicing, the circularization of circRNAs harboring circDesign optimized VZV gE sequences was still highly efficient. In this comparison, we included three control sequences: CV-Poka which stems from a CAI-maximized sequence (CAI = 1); CV-Ther from a public optimization tool supported by Thermo Fisher; CV-Ori refers to the original wild-type VZV strain sequence without optimization (**Extended Data Fig. 13a**). Non-denaturing agarose gel electrophoresis of circRNAs showed similar correlation of migration rate with structural compactness (**Extended Data Fig. 13b**). Circularization efficiency, thermodynamic stability and in-solution stability analysis of all circRNAs encoding VZV gE revealed a good correlation with MFE value and ensemble structure diversity (**Extended Data Fig. 13c,d&e**). As revealed by the secondary structure prediction and pairwise visualization (**Extended Data Fig. 14-17**), CV1-5 had well-defined structure and less IRES folding interruption. The protein translation level assessed by flow cytometry indicated the importance of stability factor in durable protein expression, highlighted by the MFI at 48 h post-transfection into HSkMC cells (**Extended Data Fig. 13f**). Furthermore, the *in vivo* immune responses triggered by LPP formulated circRNA VZV vaccines were evaluated in balb/c mice (n=5). CV1-5 elicited significantly higher binding antibody titers than benchmark circRNAs on day 21 and 28 (**Extended Data Fig. 18**). It was noteworthy that CV-Poka had compromised *in vitro* and *in vivo* performance despite of a maximized codon preference, in that its susceptibility to degradation as a result of high MFE value. Studies have suggested that eliciting a strong cellular mediated immune response is a key determinant for the vaccine protective efficacy against herpes zoster[43]. Therefore, we assessed the cellular immune response using ELIspot. It was inspiring to find that circDesign optimized sequences CV1-5 induced stronger VZV gE-specific T cells, which is a key determinant of VZV vaccine efficacy (**Extended Data Fig. 18d**).

Taken together, we successfully exploited the circDesign on the design of second antigen and validated the outstanding design strategy *in vitro* and *in vivo*.

Discussions

In this study, we devised a novel algorithm tool, called circDesign, for simplified circular RNA design to improve its stability as well as translatability. The usefulness of this circDesign platform was validated using RABV-G and VZV gE antigens against the benchmark designs which were designed via conventional CAI-oriented method. Here we present evidence supporting the enhanced stability and translation efficiency of circDesign optimized sequence which contributed to considerably stronger in vivo immune responses. We speculated that the sustained expression of antigens at high efficiency achieved greater antigen-specific immune activations, leading to distinguished vaccine-elicited humoral and cellular immune responses. Overall, these data demonstrated an approach for

rational circRNA design in support of next generation vaccine and therapeutic development.

The major limitation of this study lies in the fact that we performed extensive search on specific ORF sequences without further optimization of other functional regions of circRNA such as IRES motif. To the best of our knowledge, the de novo design of an efficient IRES motif remains challenging as these virally or cellularly derived IRES motifs are usually sensitive to sequence manipulation including deletion, mutation, or insertion. The different domains of IRES sequence cohesively function to recruit PIC and assemble the intact ribosome complex only when these domains are well-folded. Therefore, we did not incorporate the modulation of IRES region in the circDesign at current stage. Provided that the structure-to-activity of IRES were elucidated at molecular level, it might be possible to realized bottom-up search or optimization of IRES sequence in circDesign algorithm.

Other than IRES-driven translation from circRNA, N6-methyladenosine (m6A) modification upstream of ORF has been reported to facilitate the translation as well as the stability[44, 45]. If chemically modified nucleotides were incorporated into circRNA, it would pose difficulties on our circDesign algorithm as the structure prediction based on unmodified nucleotides is not reliable. Given that the energy model of chemically modified nucleotide is available, we would be able to do extensive structure comparison for optimal sequence design.

Materials & Methods

Ensemble diversity calculation

Ensemble diversity (ED) measures the complexity of the structural ensemble, which can be computed from pair probabilities.

$$\mathrm{ED} = \sum_{i,j} p_{ij} \times \left(1 - p_{ij}\right)$$

Positional entropy calculation

Positional entropy (PE) is a metric that measures whether a specific nucleotide at position *k* predominantly occurs in the same configuration, paired or unpaired.

$$\mathrm{PE}(k) = -\sum_{i} p_{ik} \ln p_{ik}$$

Positional entropy of the IRES region is defined as:
$\mathrm{PE(IRES)} = \sum_k \mathrm{PE}(k)$, where k is in the region of IRES. The positional entropy is 0 for a nucleotide that is always unpaired or always paired with the same partner. Thus, positions with low entropy are predicted with high confidence.

588
589 ***circRNA secondary structure prediction***
590 The circRNA secondary structure was modeled by ViennaRNA[46] with parameters
591 for circular (-p -d2 -c) RNAs. And the structure was visualized by RiboGraphViz
592 with the cirRNA secondary structure from RNAfold.
593
594 ***Vector and plasmid construction***
595 To construct a vector for circRNA synthesis, T7 promoter, homology arm,
596 elements from permuted intron-exon (PIE) construct, spacer, IRES, and coding
597 sequences were synthesized by General Biol and cloned into pUC57-mini plasmid.
598 For linear RNA synthesis, the pUC57 plasmid vector containing T7 promoter, 5'
599 UTR, Kozak sequence, coding region, 3' UTR and polyA tail was synthesized by
600 General Biol. All the sequences coding Firefly Luciferase (FLuc), RABV-G and
601 VZV-gE are supplied in supplemental materials.
602
603 ***Plasmid DNA synthesis and linearization***
604 pDNA was transformed into *E. coli* (Tsingke Biotechnology) and cultured in 100
605 mL of Luria Broth (LB) with 100 mg/mL Ampicillin (Sangon Biotech, CN).
606 Plasmid was purified using a NucleoBond Xtra Midi kit (MN) and the
607 concentration and purity was measured on a NanoDrop One (Thermo Fisher).
608 pDNA was linearized using SapI restriction enzyme for 3 h at 37 °C and purified
609 as template. After sequencing verification, the products were stored at -20 °C and
610 were used as templates for *in vitro* transcription (IVT).
611
612 ***In vitro transcription and circularization of RNA***
613 For the chemically modified linear mRNA synthesis, *in vitro* transcription
614 reaction with 100% N1-methylpseudouridine (Hongene Biotech) substitution was
615 conducted at 30 °C for 16 hours. mRNA was co-transcriptionally capped using
616 m7(3'OMeG)(5')ppp(5')(2'OMeA)pG capping reagent (Hongene Biotech) in a
617 "one-pot" reaction followed by digestion with DNase I (Thermo Fisher). Linear
618 mRNA was purified using Dynabeads MyOne Carboxylic Acid beads (Thermo
619 Fisher).
620
621 For the circular RNA synthesis, The linear RNA precursor transcripts were
622 produced using 1 μg of linearized DNA template in a MEGAScript™ reaction
623 (Ambion) for 16 h at 30 °C, according to the manufacturer's protocol. Then RNA
624 was treated with DNase I (Thermo Fisher) for 60 min at 30 °C, followed by
625 lithium chloride precipitation. To obtain circularized RNA, GTP was added to a
626 final concentration of 2 mM along with a buffer including magnesium (50 mM
627 Tris-HCl, (pH 8.0), 10 mM $MgCl_2$, 1 mM DTT; Thermo Fisher). RNA was then
628 heated to 55 °C and held for 45 min before purification using Dynabeads MyOne
629 Carboxylic Acid beads (Thermo Fisher).
630

Liquid chromatography purification of circRNA

Circular RNA products were further purified *via* liquid chromatography to remove spliced introns and precursor linear mRNA using a 21.2×300 mm size-exclusion column (SEC) with a particle size of 5 μm and pore size of 1000 Å (Sepax Technologies). RNA was run on an AKTA avant 150 purifier system in RNase-free 150 mM phosphate buffer (pH = 6.0). Purified circRNA products were concentrated by lithium chloride precipitation and analyzed using Agilent 2100 bioanalyzer.

CircRNA sequence identification

To validate the circularization of RNA, the SEC purified RNA was reverse transcribed into cDNA using a HiScript III All-in-one RT SuperMix Perfect kit (Vazyme), followed by PCR with primers that can amplify transcripts across the splicing junction site. The PCR products were sequenced using Sanger sequencing to validate the back-splicing junction of the circular RNA.

Circularization efficiency comparison

To compare the circularization efficiency after circularizing reaction before SEC purification, two sets of primers were used in qPCR method. One set of primers was designed at 3 'intron, representing the part of RNAs that without successful circularization ; the other set of primers was designed at the junction site, representing the circRNAs formed by successful circularization. Therefore, the circularization efficiency of different RNAs was obtained by comparison, and the sequence of primers was as follows：

circ-Rabies-F (5'-3'): ACAAACGGCTATTATGCGTTACC;
circ-Rabies-R (5'-3'): GACTTGAACCCACACGACCG;
Linear-Rabies-F (5'-3'):AACGTCAAGACGAGGGTAAAGAGAG
Linear-Rabies-R (5'-3'):GACTTGAACCCACACGACC
circ-VZV-F (5'-3'): TAGCTCATGCTTGGTTAGAGCAG;
circ-VZV-R (5'-3'): CCCCCTGGGAGTCGAACC;
Linear-VZV-F (5'-3'):CGGCACCCACCTAAGGCAAAC;
Linear-VZV-R (5'-3'):CGAACCCAGCACCAACGGATTC;

To calculate the Circularization efficiency of each sequence:

$$\frac{\text{power}[2, -(x-y)] \times 100\%}{\text{power}[2, -(x-y)]+1}$$

x: Ct of circular RNA, y: Ct of linear RNA

Cell culture & circRNA transfection

Human embryonic kidney 293 (HEK293, ATCC)/Human Skeletal Muscle Cells (HSkMC, ATCC) and Baby hamster kidney 21 (BHK-21, ATCC) were cultured in complete Dulbecco's Modified Eagle's Medium (DMEM, Gibco) containing 10% fetal bovine serum (FBS, Gibco) and 1% penicillin-streptomycin (Thermo Fisher). Cells were seeded in a 6-well plate at a density of 5×10^6 cells/well 24 h

674 prior to transfection. Lipofectamine Messenger MAX (Thermo Fisher) was used
675 according to the manufacturer's instructions for the transfection of circRNA.
676
677 ***Agarose gel electrophoresis of circRNA***
678 To study the electrophoretic mobility profile of circRNA, RNA samples
679 suspended in Ambion® RNA storage buffer (Thermo Fisher) were denatured at
680 75 °C for 5 minutes and snap –cooled on ice before loaded onto 1% agrose gel
681 (130 V for 1 h at room temperature). DL5000 DNA marker (Vazyme) was used in
682 the gel. Gel image was taken by Gel Doc XR+ Gel Documentation System (Bio-
683 Rad).
684
685 ***In-solution stability assay of circRNA***
686 To assess the In-solution stability of mRNA, samples were incubated in PBS
687 buffer containing 10 mM Mg^{2+} . Sampling was conducted at different time points
688 (0, 1, 2, 4, 8, 12, 16, 24, 32, 48 and 60 hours). RNA integrity was analyzed by
689 Qsep100™ Capillary Electrophoresis System (BiOptic Inc). The integrity was
690 represented as the proportion of full-length mRNA calculated on
691 electropherogram. The data were normalized to time point 0 h.
692 To extrapolate the half-life of each sequence, one-phase decay equation:
693 $$Y = (Y_0 - \text{Plateau}) \cdot e^{-KX} + \text{Plateau}$$
694 was used to fit the curve. The Y_0 and Plateau were set as 100 and 0, respectively.
695 Half-life was computed as ln(2)/K, where K refers to decay rate constant.
696
697 ***Thermodynamic stability assay of circular RNA***
698 Equal volume of circRNA (1mg/mL) and diluted Quant-iT™ RiboGreen®
699 (Thermo Fisher) reagent was mixed in 1× TE buffer. A total of 20 μL mixture was
700 loaded into 384-well plate and centrifuged at 1000 rpm for 1 min before running
701 the Melting Curve program on QuantStudio 5 Real-Time PCR System (Applied
702 Biosystems). circRNA underwent a denaturing process at 95°C for 5 min with a
703 ramp rate of 0.05°C/s starting from 25°C. Then the temperature stepped down to
704 25°C with a rate of 1.6°C/s for annealing. The fluorescent intensity data at
705 different temperatures were normalized to the initial value and plotted in
706 GraphPad Prism 10.0. Sigmoidal curve was used to fit the data to extrapolate the
707 melting temperature (T_m) of each circRNA.
708
709 ***In-cell stability assay of circular RNA***
710 HSkMC cells were seeded in a 6-well plate at a density of 5×10^6 cells per well
711 24 h prior to transfection. Lipofectamine Messenger MAX (Thermo Fisher
712 Scientific) was used according to the manufacturer's instructions for the
713 transfection of circRNA. Cells were collected and and RNA was harvested and
714 purified at 3, 12, 24, 48 and 72 h after transfection using an RNeasy Mini Plus
715 kit (QIAGEN). Synthesis of first-strand cDNA from total RNA was performed

716 with HiScript® III All-in-one RT SuperMix Perfect for qPCR (Vazyme). Gene
717 specific TaqMan primers (TsingKe) amplifying the circRNA junction site were
718 synthesized as below:
719 circ-tzF (5'-3'): ACAAACGGCTATTATGCGTTACC;
720 circ-tzR (5'-3'): GACTTGAACCCACACGACCG;
721 circ-Probe (5'-3'): FAM-ACGGACTTAAAATCCGTTGAC-MGB
722 Target amplification sequence was inserted into plasmid as an internal standard to
723 obtain the absolute circRNA copies from RNA extracts. The qPCR reaction was
724 carried out using Probe qPCR Mix kit (Takara) . For each sample, threshold cycle
725 values (Ct) were processed according to the comparative Ct method. Gene
726 expression levels were presented relative to Standard curve.
727
728 ***In vitro innate immunogenicity assay***
729 24 hours post transfection of circRNA into C2C12 cells (ATCC), cell culture
730 supernatant was collected. Interferon Beta level in supernatant was assayed by
731 VeriKine TM Mouse IFN Beta ELISA Kit (PBL assay science) according to
732 manufacurer's instruction. Optical density (OD) was measured at 450 nm using
733 Bio-Tek Synergy I plate reader. The concentration of IFN-β was deduced from the
734 standard curve.
735
736 ***Flow cytometry***
737 24 hours post transfection of circRNA, HSkMC cells were harvested and
738 resuspended in 1 mL of PBS buffer at a concentration of 1×10^7 cells/mL. 100 μL
739 of the resuspended cells was added to a FACS tube and stained with 100 μL of
740 Live/Dead Fixable Aqua Dead Cell Stain (Thermo Fisher Scientific) at a 1:100
741 dilution and human FcR blocking reagent (Miltenyi Biotec) at a 1:20 dilution on
742 ice for 30 min. Cells were then washed with 2.5 mL of FACS buffer and
743 centrifuged at 1500 rpm for 5 min. After centrifugation, cells were stained with 1
744 μg (1:100 dilution) of a anti-Rabies Virus CVS-11 antibody (Merck) or anti-VZV
745 gE mouse antibody (Abcam) at 4 °C for 30 min in dark before washing with 2.5
746 mL of FACS buffer and centrifuging at 1500 rpm for 5 min. Cells were then
747 stained with 100 μL of Goat PE-anti-mouse IgG (1:100 dilution) (Abcam) at 4 °C
748 for 30 min in dark. After incubation, cells were washed with 2.5 mL of FACS
749 buffer, centrifuged at 1500 rpm for 5 min and resuspended with 250 μL of PBS.
750 Samples were analyzed on BD Canto II (BD Biosciences). Data were processed
751 using FlowJo V10.1 (Tree Star).
752
753 ***RNA sequencing and ribosome profiling of circular RNA***
754 At 6 h post-transfection of CR-Novo and CR3 into HEK293 cells, cycloheximide
755 (Sigma) was added to cell culture medium to a final concentration of 100 μg/ml
756 to arrest protein synthesis and preserve ribosome-mRNA interaction. After a 2-
757 min incubation at 4 °C and lysis, the cell lysate was centrifuged at 3,000×g and
758 the supernatant containing free polysomes was decanted. To prepare ribosome

759 footprints (RFs), RNase I (NEB) and DNase I (NEB) were added to lysate and
760 was then incubated at room temperature on a Nutator mixer. Nuclease digestion
761 was stopped by adding SUPERase·In RNase inhibitor (Ambion)followed by
762 purification using size exclusion columns (GE Healthcare). Next, 10% (wt/vol)
763 SDS was added to the elution, and RFs with a size greater than 17nt was isolated
764 according to the RNA Clean and Concentrator-25 kit (Zymo Research). After
765 obtaining ribosome footprints, Ribo-seq libraries were constructed using
766 NEBNext® Multiple Small RNA Library Prep Set for Illumina® (catalog
767 no.E7300S, E7300L). Briefly, adapters were added to both ends of RFs, followed
768 by reverse transcription and PCR amplification. The 140-160bp size PCR
769 products were enriched to generate a cDNA library and sequenced using Illumina
770 HiSeqTM X10 by Gene Denovo Biotechnology Co. (Guangzhou, China).
771
772 ***Ribosome footprint data processing and alignment***
773 Low quality reads were filtered by fastp. Raw reads containing over 50% of low-
774 quality bases or over 10% of N bases were removed. Adapter sequences were
775 trimmed. Reads with length between 20-40 bp were retained for subsequent
776 analysis. Short reads alignment tool Bowtie2 was used for mapping reads to
777 ribosome RNA (rRNA) database, GenBank, Rfam database. The reads mapped to
778 rRNAs, transfer RNAs (tRNA), small nuclear RNAs (snRNA), small nucleolar
779 RNAs (snoRNA), and miRNA were removed. Processed RNA-seq reads were
780 aligned to the circular RNA using sequence alignment by STAR with 2-pass
781 setting enabled. The reads were assigned to different functional regions (IRES,
782 CDS, spacer, homology arm and exon) based on the position of the alignment.
783 Translation efficiency (TE) was calculated as the base 2 logarithmic ratio of
784 normalized RPFs over the normalized input for each ORF.
785
786 ***Pause sites analysis***
787 Because the translocation of ribosomes occurs along the mRNA one codon at a
788 time, the potential of single-codon resolution pauses were investigated. Using
789 PausePred (https://pausepred.ucc.ie/) which infers the locations of ribosome
790 pauses, global single codon pauses were analyzed.
791
792 ***Quantification of read abundance***
793 Reads counts in the different regions of circular RNA was calculated by software
794 RSEM, and the level was normalized by using FPKM (fragment per kilobase of
795 transcript per million mapped reads) method, and the formula is shown as follows:
796 $$FPKM = 10^6C/(NL/10^3)$$
797 Given FPKM (A) to be the abundance of sequence A, C to be number of fragments
798 mapped to sequence A, N to be total number of fragments that mapped to
799 reference sequences, and L to be number of bases on sequence A. Therefore, the
800 calculated FPKM can be directly used for comparing the difference of abundance

among samples. The ribosome footprint depth was plotted in a circular form with each functional region denoted in different color.

Polysome profiling of circRNA

At 6 h post-transfection of CR-Novo and CR3 into HEK293 cells, cycloheximide (Sigma) was added to cell culture medium to a final concentration of 100 μg/ml to arrest protein synthesis and preserve ribosome-mRNA interaction, and the cells were incubated at 37 ° C for 15 minutes. After trypsin digestion (0.25%), harvest and wash cells with ice-cold PBS supplemented with 100 mg/mL cycloheximide. The frozen tubes were flash frozen in liquid nitrogen and then stored at -80°C for later use. Samples were sent to NKY-GuangZhou Gene reader Bio-Medical Technologies Co., Ltd. (Guangzhou, China) for isolation. In brief, cells were lysed in lysis buffer (10 mM Tris-HCl pH 7.4, 150 mM NaCl, 5 mM $MgCl_2$, 1% Triton X-100, 0.5% deoxycholate, 2 mM DTT) supplemented with 4 U/mL RNase inhibitor, 100 μg/mL cycloheximide, and proteinase inhibitor cocktail (Roche, Basel, Switzerland) on ice for 20 min. After centrifugation at 13,000 g for 10 min, the supernatant was then taken and loaded into a 10% to 45% sucrose gradient solution and centrifuged at 360000 rpm for 3 h (Beckman Optima XE-100). 18 fractions from each sample were collected using a piston gradient fractionator (Biocomp, Fredericton, Canada) equipped with a Bio-Rad Econo UV monitor, followed by total RNA extraction from each fraction for RT-qPCR analysis.

Preparation of LPP-circRNA

LPP nanoparticles were prepared by a two-step method as previously described[35]. Briefly, a cationic polymer compound (PbAE) was dissolved in PBS buffer solution (pH=5.2) and circRNA was diluted with citrate buffer（pH4, 5 mM ）and RNase-free water. mRNA/PbAE complexes were prepared by a microfluidic mixer (Inano D, Micro&Nano Technology Inc, China) at a volume ratio of 5:1 (mRNA: PbAE). After that, lipids were dissolved in ethanol at molar ratios of 40:15:43.5:1.5 (ionizable lipid: 1,2-dioleoyl-sn-glycero-3-phosphoethanolamine (DOPE):Cholesterol: PEG-lipid). The lipid mixture was combined with mRNA/PbAE complexes at a ratio of 3:1 (aqueous: ethanol) using a microfluidic mixer. Formulations were concentrated using Amicon ultra centrifugal filters (EMD Millipore) in sodium acetate with 10% sucrose buffer, passed through a 0.22-mm filter, and stored at 4°C.

Nanoparticle characterization

The size, polydispersity index (PDI) and zeta potential of LPP formulated circRNA were measured by dynamic light scattering (DLS) (Malvern, Zetasizer Nano ZS). Briefly, LPP-circRNA samples were diluted in sodium acetate with 10% sucrose buffer at a concentration of 0.1 mg/mL. The measurement was performed in triplicate with 8 runs in each measurement.

843
844 ***In vitro storage stability assay of LPP formulated circRNA***
845 LPP formulated circRNA was stored in sodium acetate with 10% sucrose buffer
846 at 4°C over a time course of 60 days. At Day 0, 30 & 60, LPP-circRNA was
847 sampled for physicochemical characterization including mRNA content,
848 hydrodynamic size and PDI.
849
850 ***Cell count Kit-8 (CCK-8) assay of LPP formulated circRNA***
851 Cell proliferation capacity was evaluated using CCK-8 assay kit (Sigma Aldrich)
852 according to the manufacturer's instructions. Briefly, HSkMC cells were seeded
853 into 96-well plates at a density of 5×10^5 cells/well. On the other day, 100 ng of
854 LPP formulated circRNA was added into cell culture directly. At 48 h post-
855 transfection, 10 μL CCK-8 solution was added to each well and cells were
856 incubated for a further 2 h at 37 °C. Optical density (OD) was measured at 450
857 nm using Bio-Tek Synergy I plate reader.
858
859 ***mRNA concentration and encapsulation efficiency of LPP-mRNA***
860 LPP formulated circRNA was diluted with 1×TE buffer followed by mixing with
861 an equal volume of 2% Triton X-100 and incubated at RT for 20 min to release
862 the encapsulated mRNA-circRNA core. 100 μL of each sample was then
863 transferred to the wells of a 96-well plate, to which 100 μL of 200 × diluted
864 RiboGreen™ RNA Reagent (Thermo Scientific) was added. The plate was shaken
865 and incubated at RT for 10 min. After that, the fluorescence of the plate was read
866 by a Bio-Tek Synergy I plate reader (BioTek). A series of diluted standards were
867 also prepared corresponding to 0.1–2.0 μg/mL mRNA. A standard curve of
868 fluorescence as a function of mRNA concentration was plotted by linear
869 regression, from which the mRNA concentrations of the samples were calculated.
870 Encapsulation efficiency was calculated as Encapsulation efficiency (%) = [(total
871 mRNA - free mRNA)/total mRNA] × 100%.
872
873 ***LPP formulated circRNA protection assay***
874 Content analysis was performed to evaluate the integrity of the RNA after the
875 formulation process and to assess RNase protection of the encapsulated RNA. For
876 the RNase protection assay, 1 mAU of RNase A (Thermo Scientific) per
877 microgram of RNA were added to the LPP/LNP/RNA formulation for 30 min at
878 room temperature. RNase was then inactivated by incubating the sample with 1.68
879 mAU/μg RNA of proteinase K (Thermo Scientific) at 55 °C for 10 min. After
880 RNase inactivation, residual RNA was detected from formulations (as
881 described in the *mRNA concentration and encapsulation efficiency of LPP-mRNA*
882 above).
883
884 ***Fluorescent microscopy imaging of circRNA expression***
885 For the experiments where eGFP-mRNA was transfected, 5×10^5 HSkMC cells

were incubated with 2 μg of eGFP-mRNA packaged in LPP or lipofectamine (Thermo Scientific) for 24 h in 6-well plate, and eGFP expression was visualized using an Eclipse DMi8 fluorescent microscope (Leica). Frequency of eGFP-expressing cells was determined using flow cytometry (BD FACSCanto II, Becton Dickinson). The excitation and emission was set at 488 nm and 525 nm, respectively.

In vivo biodistribution of FLuc encoded LPP-circRNAs in mice

Female balb/c mice aged 6-8 weeks were purchased from Shanghai Model Organisms Center. 5 μg of LPP formulated circRNA or linear RNA encoding Firefly Luciferase (FLuc) in PBS were administrated into mice (n=3 for each group) intramuscularly with 3/10 insulin syringes (BD biosciences). Mice were then anesthetized for whole-body bioluminescence imaging with an IVIS Spectrum (Roper Scientific) at different time points (6h, 24h, 48h, 72h, 96h and 192h).

Administration of LPP circRNA vaccine in mice

For immunogenicity studies, female balb/c mice (Shanghai Model Organisms Center) aged 6-8 weeks old (n=5 for each group) were used. 2 μg of LPP formulated circRNA vaccines were diluted in 50μL 1×PBS buffer and intramuscularly administrated into the mice's same hind leg for both prime and boost shots at an interval of two weeks. Mice in the control groups received PBS. The blood samples were collected on Day 10, 14, 21 & 28 post prime dosing. Mice spleens were also harvested at the endpoint (D28) for ELISpot and flow cytometry.

pVNT measurement

A pseudovirus neutralization assay was performed to evaluate the neutralizing ability of sera collected from immunized mice as described previously[ref]. In brief, serially diluted antibodies were first incubated with pseudotyped virus (Beijing Tiantan Biological) for 1 h, and the mixture was then incubated with BHK-21 cells. After a 24-h incubation in an incubator at 37 °C, cells were collected and lysed with luciferase substrate (PerkinElmer), then underwent luminescence intensity measurement by BioTek microplate reader. The IC50 value was calculated using 4 parameter logistic non-linear regression.

Enzyme-Linked ImmunoSorbent Assays (ELISA)

Briefly, recombinant VZV gE protein (Genscript) diluted in coating buffer (Biolegend) were used to coat 96-well EIA/RIA plates (Greiner Bio-one, 100 ng/well) at 4°C overnight. The plates were then washed with 1× PBS-T (0.05% Tween-20) and blocked with 2% BSA in PBS-T for 2 hours at RT. Mice sera samples with serial dilutions were added and incubated for 2 hours at RT. After washing, HRP-conjugated goat anti-mouse IgG Ab (1:10,000) was added and

929 incubated for 1 hour. TMB substrate (Invitrogen) was then used for color
930 development and the absorbance was read at 450 nm using BioTek microplate
931 reader. Endpoint titers were calculated as the largest sample dilution factor
932 yielding a signal that exceeds 2.1-fold value of the background.
933
934 ***In vivo mouse cytokine analysis***
935 A serial dosage of LPP formulated CR3, CR-Novo and LR-Novo (0.02 μg, 0.2 μg,
936 2 μg) were intramuscularly administered into female Balb/c mice (n=5, Shanghai
937 Model Organisms Center) aged 6-8 weeks old. Mice sera were collected retro-
938 orbitally at 4 h and 7 days post administration and subjected to cytokine analysis
939 (Cytometric Bead Array Mouse Inflammation Kit, BD) using flow cytometry
940 following the manufacturer's instructions. Data were presented as the percentage
941 change relative to baseline mice group administered with PBS.
942
943 ***IFN-γ ELISpots***
944 Assessment of the IFN-γ T cell response was performed using the Mouse IFN-γ
945 ELISpotPLUS kit (Mabtech) following the manufacturer's instructions. Briefly,
946 anti-IFN-γ pre-coated plates were blocked with DMEM+10% FBS for at least 30
947 min, then cells were added at 3×10^5 cells per well for negative control (media
948 only) and RABV-G or VZV-gE peptide pools (15-mers overlapping by 11;
949 Genscript) (1 μg/mL) in 200 μL final volume per well. The positive control wells
950 contained 5×10^4 cells per well in 200 μL final volume per well with 5 μg/mL of
951 ConA. Plates were incubated overnight at 5% CO_2, 37 °C incubator and developed
952 as per the manufacturer's protocol. After overnight stimulation, plates were
953 washed and sequentially incubated with biotinylated IFN-γ detection antibody
954 (R4-6A2), streptavidin-ALP, and finally BCIP/NBT. Plates were imaged with
955 ImmunoSpot Analyzer and quantified with ImmunoSpot software.
956
957 ***Biodistribution of LPP-circRNA***
958 The mice were divided into two groups, and 5 μg CR-Novo-LPP or CR3-LPP was
959 injected into the hind legs, respectively. 5 mices in each group were euthanized at
960 2h, 6h, 24h, 48h, 72h and 168h after administration. Tissue samples including
961 heart, liver, spleen, lung, kidney, small intestine, brain, muscle at the injection site,
962 and lymph node were collected and rapidly frozen in liquid nitrogen, and RNA
963 was extracted using trizol method. The levels of CR-Novo or CR3 in tissue
964 samples were analyzed by RT-qPCR. GraphPad Prism 8 and Origin2021 software
965 were used for data processing.
966 Gene specific TaqMan primers amplifying the circRNA junction site were
967 synthesized (TsingKe) as below:
968 circ-tzF (5'-3'): ACAAACGGCTATTATGCGTTACC;
969 circ-tzR (5'-3'): GACTTGAACCCACACGACCG;
970 circ-Probe (5'-3'): FAM-ACGGACTTAAAATCCGTTGAC-MGB
971 Target amplification sequence was inserted into plasmid as an internal standard to

obtain the absolute circRNA copies from RNA extracts. The qPCR reaction was carried out using Probe qPCR Mix kit (Takara). For each sample, threshold cycle values (Ct) were processed according to the comparative Ct method. Gene expression levels were presented relative to Standard curve.

Correlation analysis

The Pearson correlation coefficient was calculated to assess the relationship between continuous variables, for example, experiment half-life and MFE.

Statistical Analyses

Two-tailed Student t test was used to determine statistical significance for data comparisons at a single time point. One-way ANOVA was used to determine statistical significance for data comparisons with multiple time points. Prism version 8.0 (GraphPad) or Origin 10.0 were used for generation of all graphs and performance of statistical analyses. Statistical significance is denoted as ns, not significant, *$p < 0.05$, **$p < 0.01$, and ***$p < 0.001$.

Data Availability

The RNA sequences and DNA primer sequences used in the biological experiments are included in the Supplementary Sequence Information section (at the end of the manuscript). and are also uploaded in the submission system. We will release data at a permanent location upon acceptance and the accession codes will be available before publication.

Code Availability

The code has been submitted as part of this submission and will be released at a permanent location upon acceptance.

Conflict of Interest

L.H. is the founder of Coderna.ai. C.X., W.W., Y.T., H.S., Y.Y., Q.W., H.S., and H.L. are employees of StemiRNA Therapeutics. C.X., W.W., Y.T., H.S., and H.L. have filed provisional patents for the circRNA rabies and VZV vaccines.

Author Contributions

H.L. conceived and directed the project. H.L., H.S. and C.X. supervised all the *in vitro* and *in vivo* experiments. L.Z. and L.H. developed the circDesign algorithm to design circRNA sequences. C.X., W.W., X.W. and J.A. performed the mRNA synthesis and gel electrophoresis experiments. H.X., X.Q. and M.S. performed the liquid chromatography analysis and purification. C.X., W.W., J.A., X.S., Y.Y. and H.S. performed the protein expression and *in vivo* assays, and Q.W. conducted

LPP formulation and chemical stability assays. Y.T. performed the ribo-seq experiments. H.Z. and Y.G. performed the animal study including injection and *in vivo* imaging. C.X., L.Z., H.L., H.S., W.W., Y.T., Q.W., and L.H. wrote the manuscript.

Acknowledgements

We thank the assistance from colleagues including Xinxin Su, Mingyang Liu, and Kun Xie at StemiRNA Therapeutics in animal experiments. Congcong Xu is sponsored by Shanghai Pujiang Talent Program (22PJ1423100). The funds from StemiRNA Therapeutics were supported by the Science and Technology Commission of Shanghai Municipality, China (20S11909100, 22S11902300; Shanghai Strategic Emerging Industry Development special fund (ZJ640070216) and the project of mRNA Innovation and Translation Center, Shanghai, China.

Figure Legends

Figure 1. circDesign approach overview and design of circular RNA molecules encoding RABV-G. a, circDesign workflow illustration from library screening to structure-based analysis. Given a specific amino acid sequence, mRNA sequence pool was generated followed by candidate screening based on MFE and CAI. By incorporation of ORF into circRNA backbone, the circRNA folding, ensemble diversity and cross-region interaction was assessed. The designed circRNAs were then evaluated in vitro and in vivo. b, Distribution of circDesign-generated ORFs (R1-R6) and benchmark sequences (Ther & Novo) in a two-dimensional plot. The color darkness indicates the ensemble diversity. Schematic illustration of circRNA sequence designs composed of different functional regions for circularization. Homo arm refers to homology arm for 5'- & 3'- end pairing. c, Representative circularized diagram showing the CR3 and CR-Novo sequence. d, Secondary structure of CR3 and CR-Novo (uncolored: IRES motif; red: loop structure; blue: stem structure). e, Pairwise visualization of CR3 and CR-Novo showing the intra- and inter-region interaction (red: inter-region interaction; blue: inter-region interaction). Each region was colored as indicated.

Figure 2. Characterization of circular RNA molecules encoding RABV-G. a, Comparison of the circularization efficiency of different circRNA using qPCR method. Data in triplicate were presented as mean ± s.d. b, Native agarose gel characterization of the circRNA showing the correlation of gel mobility with circRNA folding compactness. c, Thermodynamic stability of circRNA molecules suggesting a correlation of MFE with melting temperature. The mean values of three independent measurement data were fitted with sigmoidal curve to

extrapolate the melting temperature. d, In-solution degradation curve of circRNA upon incubation in PBS buffer containing 10 mM Mg^{2+} at 37 °C. Triplicate data were presented as mean ± s.d. and fitted with one-phase decay curve to obtain half-life and decay constant. e, In-cell degradation of all circRNAs within 72 h post-transfection in HSkMC cells. Triplicate data points were presented as mean ± s.d. followed by non-linear one-phase decay fitting. The original value at the 0 h was set as 125% with a final plateau value at 0%. f, Flow cytometry analysis of circRNA in comparison with linear RNA in HSkMC cells at 24 h post-transfection. Mean fluorescent intensity (MFI) of protein expression level from cells transfected circRNA or linear mRNA was calculated. Three independent measurement data were plotted as mean ± s.d. One-way ANOVA with multiple comparisons to LR-Novo group was performed for statistical analysis. g, Correlation analysis of MFE with experiment in-solution and in-cell half-life. h, Correlation analysis of predicted half-life with experiment half-life.

Figure 3. Translation efficiency comparison of CR3 and CR-Novo. Predicted secondary structure of a) CR3 and b) CR-Novo. c, Simplified workflow diagram of ribosome profiling and polysome profiling of circRNA. d, Abundance of Ribo-seq and RNA-seq counts of circRNA (CR3 & CR-Novo) in transfected cells showing the higher translation efficiency of CR3. d, Total RNA-seq and Ribo-seq fpkm of CR-Novo and CR3 showing the relatively higher RNA abundance and higher ribosome footprint counts in cellular context. e, circular barplot showing the ribosome footprints of CR3 and CR-Novo. h, Polysome profiling results of CR3 and CR-Novo. f, Total polysome profiling of CR3 (black) and CR-Novo (red) transfected cells. g, RT-qPCR quantification of CR3 (black) and CR-Novo in collected ultracentrifuge fractions. The colored region refers to different major fractions from 40S, 60S, 80S (monosome) to polysomes. Data in triplicate measurement were presented as mean ± s.e.m.

Figure 4. Characterization of LPP formulated circRNAs. a, Scheme of two-step manufacturing of LPP formulated circRNA. The lipid mixture contains ionizable lipid, PEGylated lipid, cholesterol and helper lipid. b, The hydrodynamic size and polydispersity index (PDI) of LPP formulated linear RNA (LR-Fluc) and circular RNA (CR-FLuc). Zeta potential of LPP formulated circRNA and linear RNA. Three independent measurement data were plotted as mean ± s.e.m. d, Representative whole-body IVIS images of mice administered LPP CR-FLuc or LR-FLuc at different time points (6h, 24h, 48h, 72h, 96h and 168h). e. Total flux curve of luminescence as a function of time in balb/c mice (n=3; Green: CR-FLuc-LPP; Pink: LR-FLuc-LPP; Grey: PBS). f, Area under the curve (AUC) calculation

of three groups from 6 h to 168 h suggesting the accumulated luciferase activity over the time course. Each dot represented the mean ± s.e.m. of data from three mice. Statistical significance was determined by One-way ANOVA multiple comparisons with LR-FLuc, ***p < 0.001; **p < 0.01; *p < 0.05; ns, not significant. g, Hydrodynamic size and PDI of LPP formulated circRNA and linear RNA. Three independent measurement data were plotted as mean ± s.e.m. h, Zeta potential of LPP formulated circRNA and linear RNA. Three independent measurement data were plotted as mean ± s.e.m. i, Storage stability of LPP formulated circRNA and linear RNA at 4°C implying the shelf life of circRNA vaccines. Samples in triplicate were treated and tested. The data to each sample were normalized to its D0 as 1 and plotted as mean ± s.e.m.

Figure 5. In vivo immune responses induced by circRNA rabies vaccine. a, Balb/c mice (n=5) immunization schedule and proposed mechanism of action of LPP circRNA rabies vaccines. Pseudovirus neutralizing titer (pVNT) of mice sera immunized with two doses of LPP formulated RNA vaccines on b) D10, c) D14, d) D21 and e) D28. pVNT data were presented as geometric mean ± geometric s.d. f, The geometric increase (GMI) of pVNT from mice vaccinated with different RNA vaccines using D10 pVNT as the baseline. GMI data were plotted with geometric s.d. g, IFN-γ ELISpot analysis of mice splenocytes on Day 28 showing robust cellular immune responses triggered by circDesign optimized sequences. Data in graph represented as s.f.c. per 3*10^5 cells. Each point on violin plot represents a single mouse. Bold black line represents the median. The significance between groups was determined using a one-way ANOVA with Dunn's multiple comparison test, ***p < 0.001; **p < 0.01; *p < 0.05; ns, not significant. s.f.c., spot-forming cells. h, Summary of pVNT results from D10 to D28 of all vaccinated balb/c mice (n=5) Data were presented as geometric mean ± geometric s.d.

Figure 6. In vivo biodistribution and immune response longevity analysis of LPP formulated rabies vaccines. In vivo biodistribution of LPP formulated circRNA. RT-qPCR quantification of a) CR-Novo and b) CR3 in different tissues at different time points (6h, 24h, 48h, 72h and 168h) in balb/c mice (n=5 per group at each time point). c, Pie plot showing the tissue distribution of circular RNA at various time points. d, Parallel comparison of circRNA abundance in muscle tissue as a function of time. Statistical significance was determined by multiple Mann-Whitney u tests ***p < 0.001; **p < 0.01; *p < 0.05; ns, not significant. e, Scheme of immunization schedule in balb/c mice study (n=5). f, Pseudovirus neutralizing antibody titer kinetics of CR3 and CR-Novo. Data were presented as geometric

mean ± geometric s.d. Statistical significance was determined by multiple Mann-Whitney u tests ***$p < 0.001$; **$p < 0.01$; *$p < 0.05$; ns, not significant. g, IFN-γ and TNF-α ELISpot analysis of mice splenocytes on Day 28 showing robust cellular immune responses triggered by CR3. Data in graph represented as s.f.c. per 3*10^5 cells. Each point on violin plot represents a single mouse. Bold black line represents the median. The significance between groups was determined using a one-way ANOVA with Dunn's multiple comparison test, ***$p < 0.001$; **$p < 0.01$; *$p < 0.05$; ns, not significant. s.f.c., spot-forming cells.

Figure 1

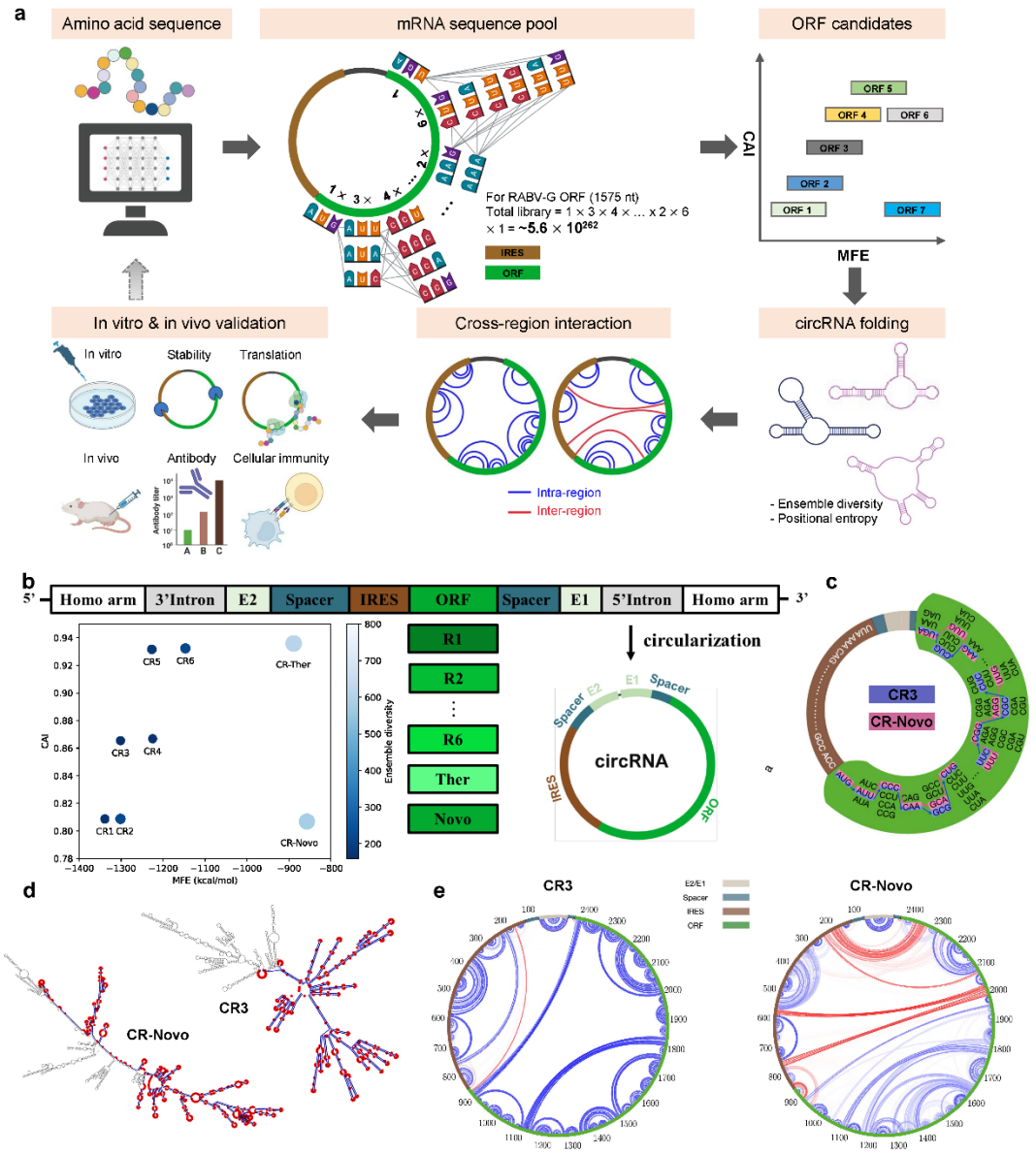

1137

Figure 2

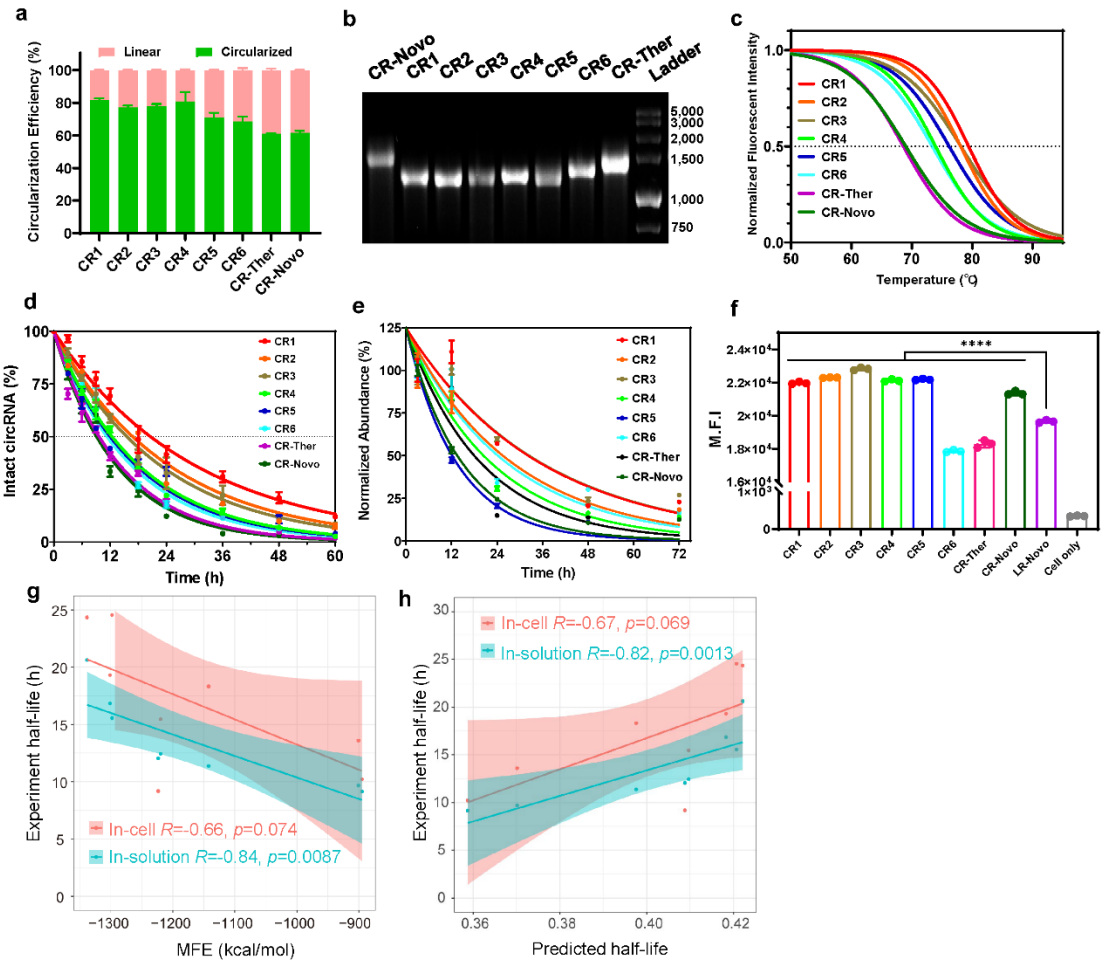

1138

Figure 3

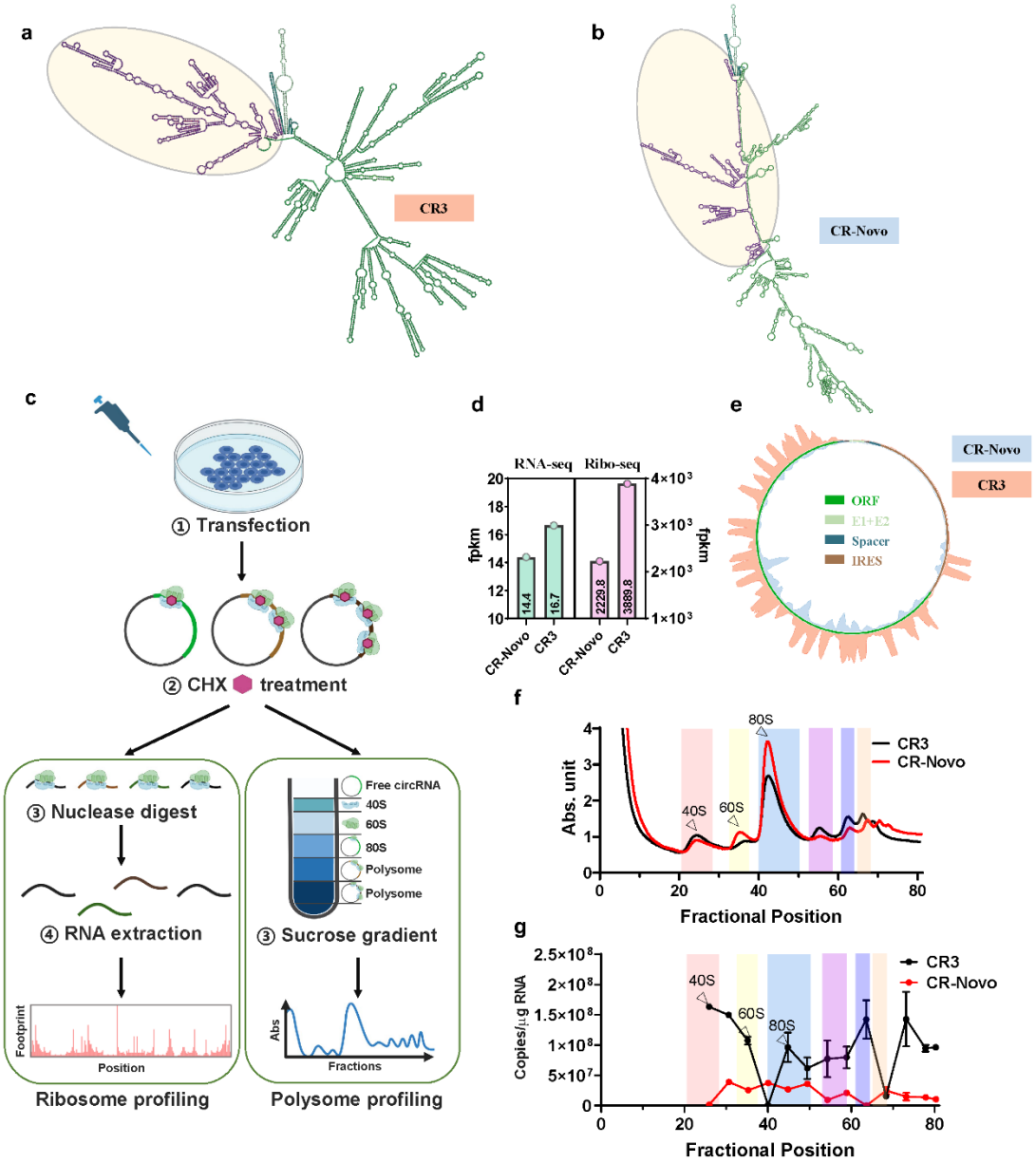

1139

Figure 4

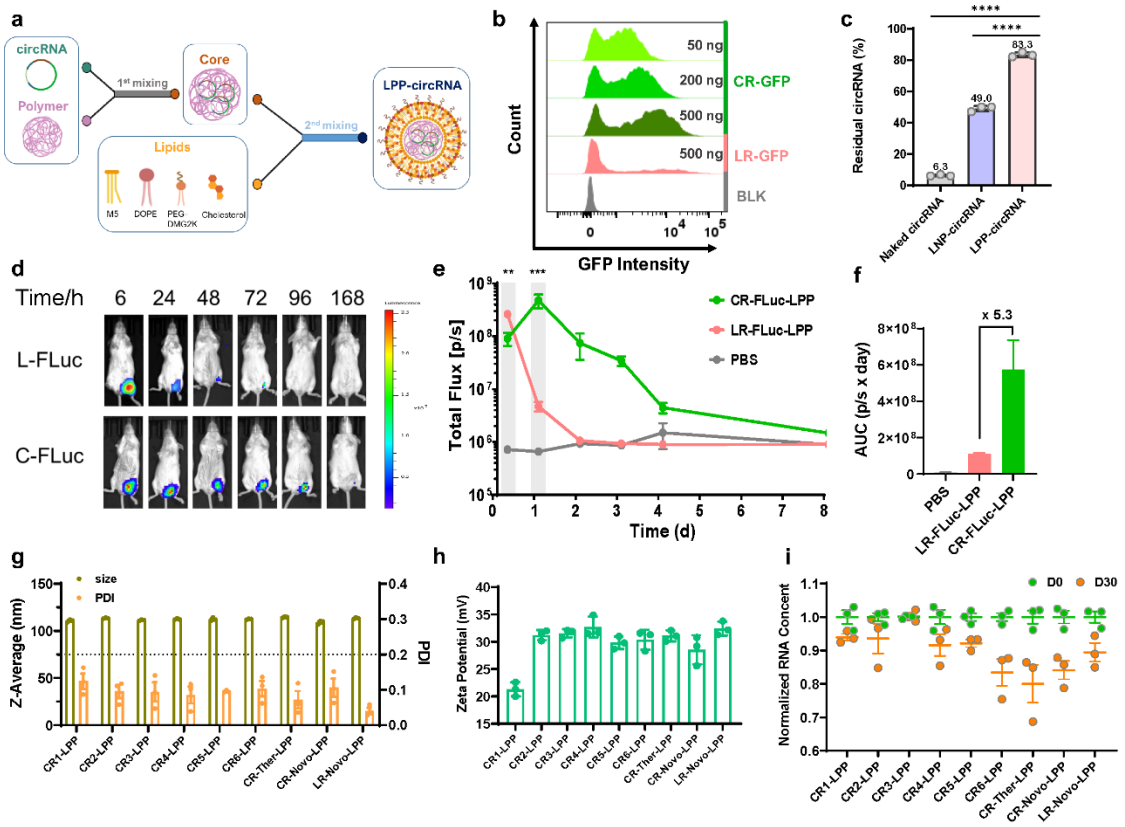

1140

Figure 5

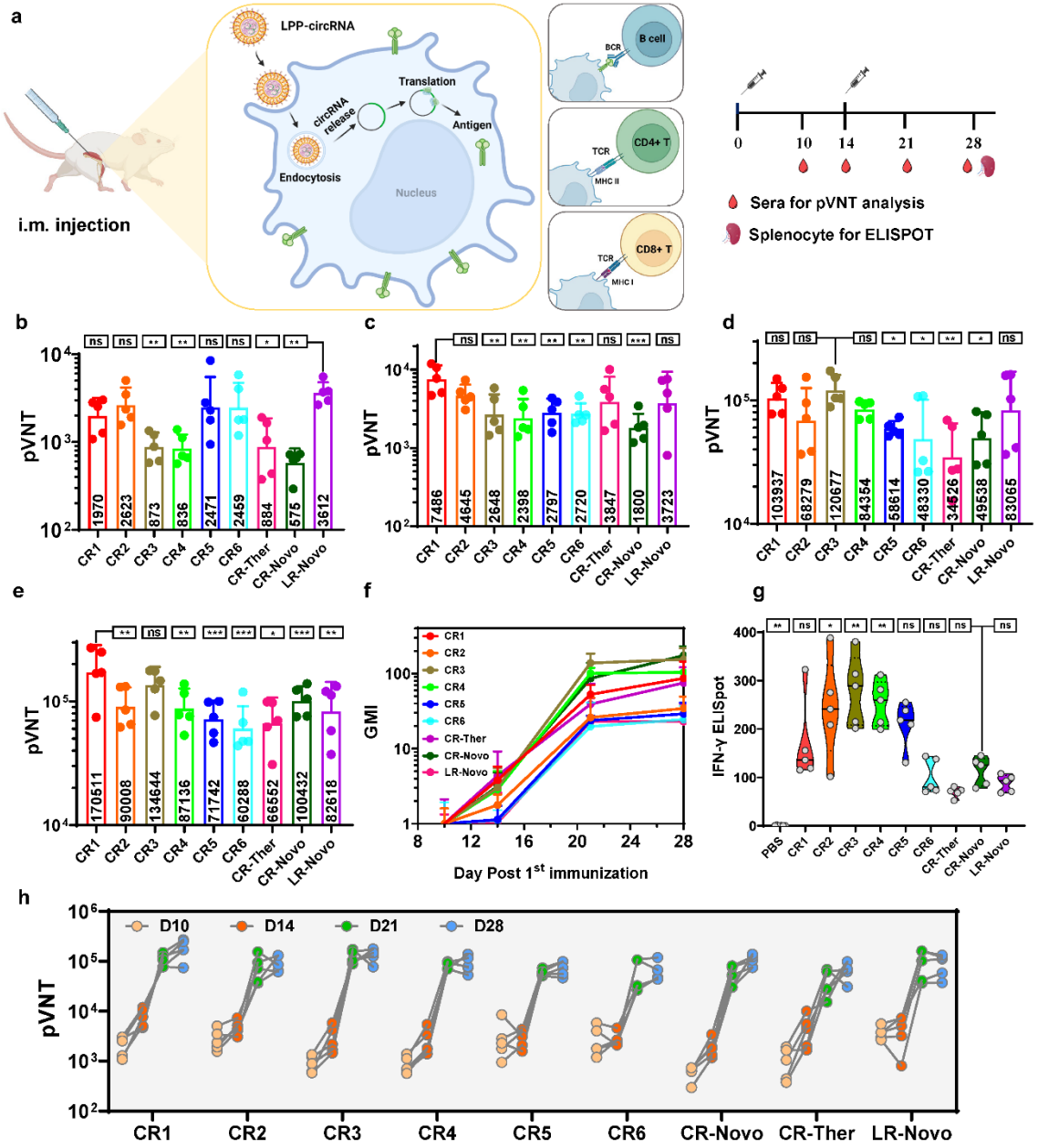

1141

Figure 6

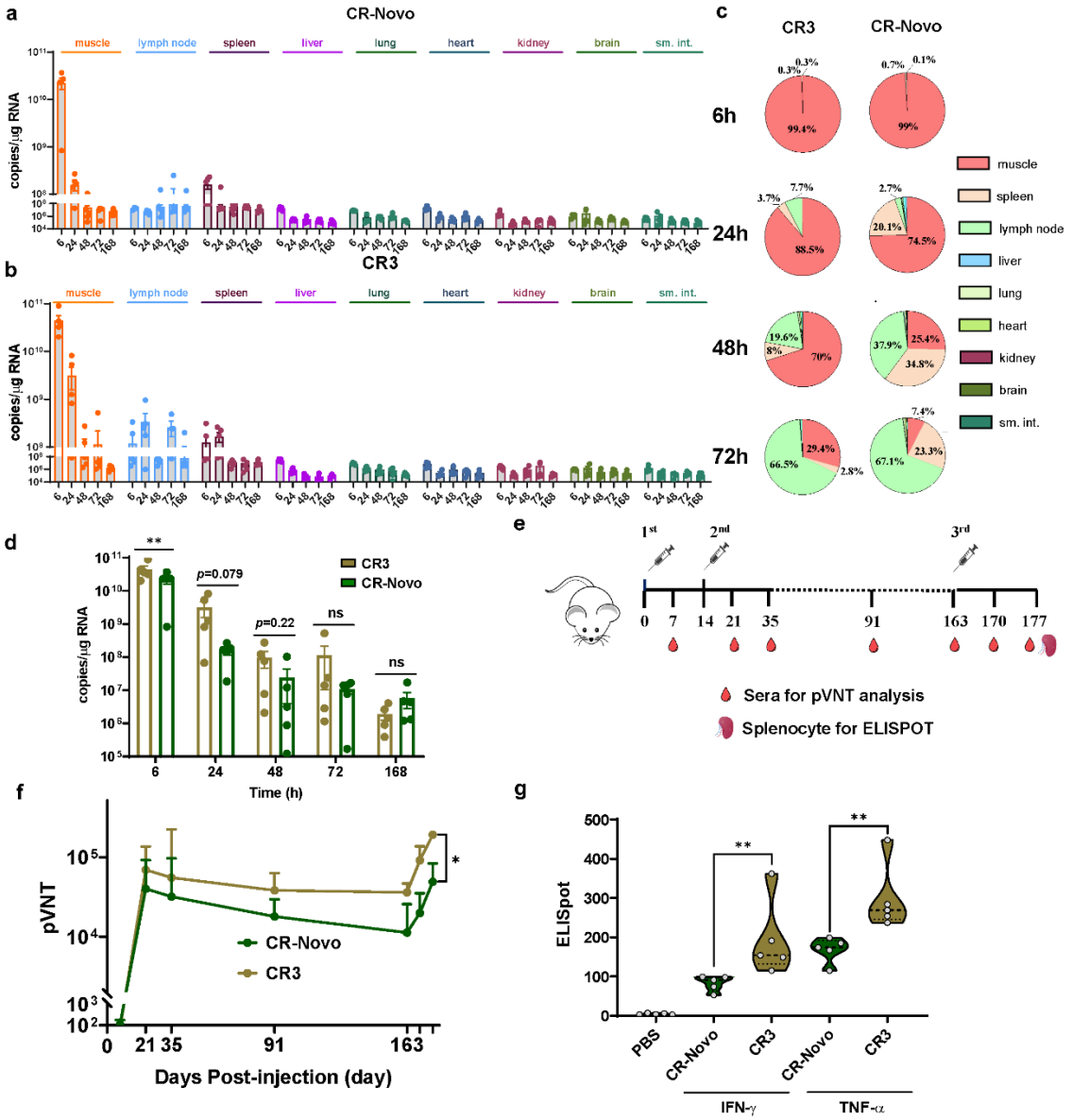

1142

1143

References

1. Leppek, K. et al. Combinatorial optimization of mRNA structure, stability, and translation for RNA-based therapeutics. *Nat Commun* **13**, 1536 (2022).
2. Trepotec, Z. et al. Maximizing the Translational Yield of mRNA Therapeutics by Minimizing 5'-UTRs. *Tissue Eng Part A* **25**, 69-79 (2019).
3. Orlandini von Niessen, A.G. et al. Improving mRNA-Based Therapeutic Gene Delivery by Expression-Augmenting 3' UTRs Identified by Cellular Library Screening. *Mol Ther* **27**, 824-836 (2019).
4. Xia, X. Detailed Dissection and Critical Evaluation of the Pfizer/BioNTech and Moderna mRNA Vaccines. *Vaccines (Basel)* **9** (2021).
5. Mauger, D.M. et al. mRNA structure regulates protein expression through changes in functional half-life. *Proc Natl Acad Sci U S A* **116**, 24075-24083 (2019).
6. Zhang, H. et al. Algorithm for Optimized mRNA Design Improves Stability and Immunogenicity. *Nature* (2023).
7. Meganck, R.M. et al. Engineering highly efficient backsplicing and translation of synthetic circRNAs. *Mol Ther Nucleic Acids* **23**, 821-834 (2021).
8. Katrekar, D. et al. Efficient in vitro and in vivo RNA editing via recruitment of endogenous ADARs using circular guide RNAs. *Nat Biotechnol* **40**, 938-945 (2022).
9. Qu, L. et al. Circular RNA Vaccines against SARS-CoV-2 and Emerging Variants. *Cell* (2022).
10. Wen, S.Y., Qadir, J. & Yang, B.B. Circular RNA translation: novel protein isoforms and clinical significance. *Trends Mol Med* **28**, 405-420 (2022).
11. Chen, C.K. et al. Structured elements drive extensive circular RNA translation. *Mol Cell* **81**, 4300-4318 e4313 (2021).
12. Chen, R. et al. Engineering circular RNA for enhanced protein production. *Nat Biotechnol* **41**, 262-272 (2023).
13. Hofacker, I.L. RNA secondary structure analysis using the Vienna RNA package. *Curr Protoc Bioinformatics* **Chapter 12**, Unit 12 12 (2004).
14. Garcia-Martin, J.A. & Clote, P. RNA Thermodynamic Structural Entropy. *PLoS One* **10**, e0137859 (2015).
15. Xia, X. An improved implementation of codon adaptation index. *Evol Bioinform Online* **3**, 53-58 (2007).
16. Schnee, M. et al. An mRNA Vaccine Encoding Rabies Virus Glycoprotein Induces Protection against Lethal Infection in Mice and Correlates of Protection in Adult and Newborn Pigs. *PLoS Negl Trop Dis* **10**, e0004746 (2016).
17. Hellgren, F. et al. Unmodified rabies mRNA vaccine elicits high cross-

1184 neutralizing antibody titers and diverse B cell memory responses. *Nat*
1185 *Commun* **14**, 3713 (2023).
1186 18. Yang, J. et al. Intratumoral delivered novel circular mRNA encoding
1187 cytokines for immune modulation and cancer therapy. *Mol Ther Nucleic*
1188 *Acids* **30**, 184-197 (2022).
1189 19. Amaya, L. et al. Circular RNA vaccine induces potent T cell responses.
1190 *Proc Natl Acad Sci U S A* **120**, e2302191120 (2023).
1191 20. Wesselhoeft, R.A., Kowalski, P.S. & Anderson, D.G. Engineering circular
1192 RNA for potent and stable translation in eukaryotic cells. *Nat Commun* **9**,
1193 2629 (2018).
1194 21. Hofacker, I.L. Energy-directed RNA structure prediction. *Methods Mol*
1195 *Biol* **1097**, 71-84 (2014).
1196 22. Mathews, D.H. Revolutions in RNA secondary structure prediction. *J Mol*
1197 *Biol* **359**, 526-532 (2006).
1198 23. Souii, A., Ben M'hadheb-Gharbi, M. & Gharbi, J. Role of RNA structure
1199 motifs in IRES-dependent translation initiation of the coxsackievirus B3:
1200 new insights for developing live-attenuated strains for vaccines and gene
1201 therapy. *Mol Biotechnol* **55**, 179-202 (2013).
1202 24. Bhattacharyya, S., Verma, B., Pandey, G. & Das, S. The structure and
1203 function of a cis-acting element located upstream of the IRES that
1204 influences Coxsackievirus B3 RNA translation. *Virology* **377**, 345-354
1205 (2008).
1206 25. Packer, M., Gyawali, D., Yerabolu, R., Schariter, J. & White, P. A novel
1207 mechanism for the loss of mRNA activity in lipid nanoparticle delivery
1208 systems. *Nat Commun* **12**, 6777 (2021).
1209 26. Crommelin, D.J.A., Anchordoquy, T.J., Volkin, D.B., Jiskoot, W. &
1210 Mastrobattista, E. Addressing the Cold Reality of mRNA Vaccine Stability.
1211 *J Pharm Sci* **110**, 997-1001 (2021).
1212 27. Jeck, W.R. & Sharpless, N.E. Detecting and characterizing circular RNAs.
1213 *Nat Biotechnol* **32**, 453-461 (2014).
1214 28. Garneau, N.L., Wilusz, J. & Wilusz, C.J. The highways and byways of
1215 mRNA decay. *Nat Rev Mol Cell Biol* **8**, 113-126 (2007).
1216 29. Guo, Y., Wei, X. & Peng, Y. Structure-Mediated Degradation of CircRNAs.
1217 *Trends Cell Biol* **30**, 501-503 (2020).
1218 30. Labno, A., Tomecki, R. & Dziembowski, A. Cytoplasmic RNA decay
1219 pathways - Enzymes and mechanisms. *Biochim Biophys Acta* **1863**, 3125-
1220 3147 (2016).
1221 31. Chen, L.L. The expanding regulatory mechanisms and cellular functions of
1222 circular RNAs. *Nat Rev Mol Cell Biol* **21**, 475-490 (2020).
1223 32. Ingolia, N.T., Brar, G.A., Rouskin, S., McGeachy, A.M. & Weissman, J.S.
1224 The ribosome profiling strategy for monitoring translation in vivo by deep

1225 sequencing of ribosome-protected mRNA fragments. *Nat Protoc* **7**, 1534-
1226 1550 (2012).
1227 33. Pringle, E.S., McCormick, C. & Cheng, Z. Polysome Profiling Analysis of
1228 mRNA and Associated Proteins Engaged in Translation. *Curr Protoc Mol*
1229 *Biol* **125**, e79 (2019).
1230 34. Brar, G.A. & Weissman, J.S. Ribosome profiling reveals the what, when,
1231 where and how of protein synthesis. *Nat Rev Mol Cell Biol* **16**, 651-664
1232 (2015).
1233 35. Yang, R. et al. A core-shell structured COVID-19 mRNA vaccine with
1234 favorable biodistribution pattern and promising immunity. *Signal*
1235 *Transduct Target Ther* **6**, 213 (2021).
1236 36. Meng, C. et al. Virus-Mimic mRNA Vaccine for Cancer Treatment. *Adv*
1237 *Ther (Weinh)* **4**, 2100144 (2021).
1238 37. Tan, Y. et al. Single-cell transcriptome atlas reveals protective
1239 characteristics of COVID-19 mRNA vaccine. *J Med Virol* **95**, e28161
1240 (2023).
1241 38. Gui, Y.Z. et al. Safety and immunogenicity of a modified COVID-19
1242 mRNA vaccine, SW-BIC-213, as a heterologous booster in healthy adults:
1243 an open-labeled, two-centered and multi-arm randomised, phase 1 trial.
1244 *EBioMedicine* **91**, 104586 (2023).
1245 39. Johnson, N., Cunningham, A.F. & Fooks, A.R. The immune response to
1246 rabies virus infection and vaccination. *Vaccine* **28**, 3896-3901 (2010).
1247 40. Venkataswamy, M.M. et al. Cellular immune response following pre-
1248 exposure and postexposure rabies vaccination by intradermal and
1249 intramuscular routes. *Clin Exp Vaccine Res* **4**, 68-74 (2015).
1250 41. Overduin, L.A., van Dongen, J.J.M. & Visser, L.G. The Cellular Immune
1251 Response to Rabies Vaccination: A Systematic Review. *Vaccines (Basel)* **7**
1252 (2019).
1253 42. Mills, D.J., Lau, C.L., Mills, C. & Furuya-Kanamori, L. Long-term
1254 persistence of antibodies and boostability after rabies intradermal pre-
1255 exposure prophylaxis. *J Travel Med* **29** (2022).
1256 43. Arvin, A.M. Humoral and cellular immunity to varicella-zoster virus: an
1257 overview. *J Infect Dis* **197 Suppl 2**, S58-60 (2008).
1258 44. Zhang, L. et al. The role of N(6)-methyladenosine (m(6)A) modification in
1259 the regulation of circRNAs. *Mol Cancer* **19**, 105 (2020).
1260 45. Meyer, K.D. et al. 5' UTR m(6)A Promotes Cap-Independent Translation.
1261 *Cell* **163**, 999-1010 (2015).
1262 46. Lorenz, R. et al. ViennaRNA Package 2.0. *Algorithms Mol Biol* **6**, 26 (2011).
1263